Lab-based X-ray micro-computed tomography coupled with machine-learning segmentation to investigate phosphoric acid leaching in high-temperature polymer electrolyte fuel cells

Josh J. Bailey[1,2], Jianuo Chen[3], Jennifer Hack[1], Maria Perez-Page[3], Stuart M. Holmes[3], Dan J.L. Brett[1], Paul R Shearing[1,]*

[1]Electrochemical Innovation Laboratory, Department of Chemical Engineering, University College London, WC1E 7JE, United Kingdom

[2]School of Chemistry and Chemical Engineering, Queen's University Belfast, BT7 1NN, United Kingdom

[3]School of Chemical Engineering and Analytical Science, The University of Manchester, M13 9PL, United Kingdom

*Corresponding author: p.shearing@ucl.ac.uk; +44 (0)20 7679 3783

Abstract

A machine-learning based approach is used to segment 14 X-ray computed-tomography datasets acquired by lab-based scanning of laser-milled, high-temperature polymer electrolyte fuel cell samples mounted in a 3D-printed sample holder. Two modes of operation, one with constant current load and the other with current cycling, are explored and their impact on microstructural change is correlated with electrochemical performance degradation. Constant-current testing shows the overall quantity of phosphoric acid in the gas diffusion layers is effectively unchanged between 50 and 100 hours of operation but that inter-electrode distribution becomes less uniform. Current-cycling tests reveals similar quantities of phosphoric acid but a different intra-electrode distribution. Membrane swelling appears more pronounced after current-cycling tests and in both cases, significant catalyst layer migration is observed. The present analysis provides a lab-based approach to monitoring microstructural degradation in high-temperature polymer electrolyte fuel cells and provides a more accessible and more statistically robust platform for assessing the impact of phosphoric acid mitigation strategies.

Keywords

High-temperature polymer electrolyte fuel cell; phosphoric acid leaching; X-ray micro-computed tomography; machine-learning segmentation; accelerated stress testing.

1 Introduction

High-temperature polymer electrolyte fuel cells (HT-PEFC) are typically composed of polybenzimidazole (PBI) membranes doped with phosphoric acid (PA)[1], wherein the polymer backbone provides mechanical integrity, and the acid endows the membrane electrode assembly (MEA) with relatively high proton conductivity (>0.1 $S.cm^{-1}$) at elevated operating temperatures (150-200 °C)[2]. Compared with their low-temperature polymer electrolyte fuel cell (LT-PEFC) analogues, typically containing hydrated perfluorosulphonic acid (often, Nafion®) membranes, HT-PEFCs are not limited to being run at 80 °C (ambient pressure) as they do not need to retain water in liquid form to be suitably hydrated for their ionic conductivity. Along with mitigating water management issues, the higher operating temperature of HT-PEFCs also suppresses the impact of fuel impurities; where LT-PEFCs are constrained mostly to running on only pure hydrogen streams, HT-PEFC systems have been developed with much greater CO tolerance[3]. Although the oxygen reduction reaction at the cathode is hindered by the presence of phosphate anions at the Pt catalyst surface[4][5], HT-PEFCs have a lower sensitivity to the sorts of contaminants found in steam reformates (H_2S as well as CO), this opens up the opportunity for combined heat and power or auxiliary power unit applications[2]. Moreover, at these higher temperatures, the electrochemical reaction kinetics are improved versus their LT-PEFCs as exchange current density increases exponentially with temperature[6].

For sufficient proton conductivity, both in the membrane and in the catalyst layers (CL), a large concentration of PA is required[7]. Although it has been shown that the maximum protonation degree of PBI by PA is reached with a doping level of 2 acid molecules per repeat unit[8], often acid doping levels of up to 6-16 are realised[9][10][11], leading to a majority of acid molecules being free and highly mobile. This encourages high proton conductivity (pure H_3PO_4 has a conductivity of around 0.650 $S.cm^{-1}$)[12] but can impede electrode reactions if the phosphate anion adsorbs at the active sites, and/or it increases mass transfer losses if gas permeation is made more difficult[7]. It has been shown that PA distribution is effectively

independent of how it is introduced, but that its quantity influences the achievable performance of the HT-PEFC MEA[7].

For many years, PA redistribution was investigated by cell-averaged methods, such as by post-mortem analysis[7][13] or electrochemical techniques[7][14][15][16][17][18]. Recently, further insight has been provided by synchrotron X-ray radiographic imaging, in both in-plane[19][20][21][22] and through-plane[23] modes. In-plane X-ray radiography identified reversible membrane swelling upon current draw[19][20][22] and attributed increased transmission in the membrane to the dilution of PA by product water[19][20][22] or crossover processes[20][22]. Through-plane studies suggested that chemical conversion of PA was accompanied by a redistribution of its derivatives as dilution alone would not explain the transmission differences observed. The work revealed heterogeneity in PA distribution after operation above 0.35 $A.cm^{-2}$, with transmission changes greater under flow-field channels than under ribs[23]. Unfortunately, in this work, it was not possible to identify if these changes originated from PA redistribution or inhomogeneous membrane swelling, highlighting the drawback common to all the radiographic investigations - the lack of the third dimension.

X-ray computed tomography (CT) involves the acquisition of radiographic projections that are collected by incrementally rotating samples, positioned between a source and detector, through regularly spaced angles. The full set of projections are processed using mathematical back-projection algorithms to give a three-dimensional reconstruction of the X-ray attenuation coefficient distribution within the sample. Eberhardt *et al.* demonstrated the first tomographic investigation of HT-PEFCs, developing grayscale-concentration calibration curves for quantifying PA in the gas diffusion layer (GDL), CL and membrane[24]. The work compared MEAs immersed in known concentrations of PA, correlating local grayscale to bulk PA concentration and its concentration in “PA + C” mixtures, whose grayscale peaks overlapped in the image histograms for all concentrations. The authors conceded that at low PA concentrations, PA and “PA + C” peaks were not separable, such that PA volume in the GDL of wet samples was estimated by a slice-by-slice subtraction method versus the GDL of a different dry sample. All images were of non-operated components at room temperature, thus

the quantities of PA in the GDLs were not representative of real operation. Follow-up *operando* studies targeted PA re-distribution under dynamic load conditions[25], monitoring PA distribution in the anode GDL as a function of current density. Increasing current density from 0.2 to 0.8 A.cm^{-2} coincided with PA flowing into the anode GDL, and a continuous path of PA between membrane and flow-field was observed after 15 min. GDL and flow-field immediately lost PA upon lowering the current, implying an inverse process at play. The original condition was not re-established, with some PA lost from the electrolyte reservoir, potentially contributing to long-term degradation. “Electrochemical pumping”, similar to that in phosphoric acid fuel cells[26], was reported to be behind PA migration from cathode to anode, resultant from $H_2PO_4^-$ migration in this direction. The average increase in grayscale on the anode side, with a small decrease on the cathode, is consistent with the pumping mechanism, but the increase in grayscale value (greater absorption) in the membrane was counter to the behaviour in prior radiographic studies[19][21][20][22].

Recently, Halter *et al.* investigated PA leaching over two current cycles, linking PA content to mass transport losses, approximating flooding times and highlighting CL cracks as the determining factor for PA egress from the membrane[27], as supported by work by Chevalier *et al.*[28]. The latter work used synchrotron X-ray CT to produce inputs for a pore network model (PNM)[29], combining with an invasion percolation algorithm[30] to predict PA mass and invasion patterns, matching well to experiment[7]. However, only one sample with an unrealistically thick CL (100-200 µm) was studied.

Although synchrotron experiments have revealed important insights into PA (re-)distribution, beamtime access is limited, time constraints mean that only a few samples are investigated in each study, and the high flux risks radiation damage to membranes. Fortunately, the recent application of lab-based X-ray micro-CT in materials science[31], among other fields[32][33], has allowed for approaches to imaging HT-PEFC in a more accessible fashion, albeit with polychromatic radiation and lower flux. An early example investigated CL morphologies from different fabrication routes but without information on PA distribution[34]. Schonvogel *et al.* explored the use of accelerated stress tests (AST), one of

which was used in this work (0.6 to 1.0 A cm^{-2} cycling), but their X-ray micro-CT images were simply used to identify CL crack, without any segmentation of the acquired tomograms, nor comprehensive analysis of the MEA in three dimensions[35]. More recent work by Halter *et al.* used PA injection methods, which rely on subtractive imaging ("dry" subtracted from "wet" images), to investigate the influence of PA concentration and temperature on the wetting behaviour of PA on GDL materials by capillary pressure and contact angle measurements[36], quantifying the capillary pressure required to see PA breakthrough the entire gas diffusion electrode (GDE), albeit for their specific materials selection and not from PA introduced into the GDE *in-situ*. A follow-up *operando* study of PA migration in HT-PEFCs with two different CL morphologies correlated their previous *ex-situ* injection work with real *operando* performance[37], showing that even at the low current densities of 0.2 A.cm^{-2}, PA is present in CL cracks, but increases significantly at higher current densities of 0.8 A.cm^{-2}.

The focus of the present study is on improving the implementation of accessible, lab-based X-ray micro-CT in the study of HT-PEFCs, with a focus on monitoring PA migration. The investigations make use of the AST procedure introduced recently[35], wherein load cycling between 0.6 and 1.0 A.cm^{-2} is used to accelerate PA leaching and allow for semi-quantitative determinations to be made from high-resolution, segmentable tomograms. Emphasis is placed on increasing the statistical robustness of X-ray lab-based CT, leveraging its greater longitudinal availability versus the synchrotron, as well as mitigating poorer contrast by acquiring tomograms from several replicates with optimised scanning parameters. The results indicate that the AST used is sufficient to bring about PA migration that can be reliably identified by lab-based micro-CT and paves the way for lab-based investigations of PA leaching mitigations in state-of-the-art HT-PEFC microstructures.

2 Materials and Methods

2.1 HT-PEFC

2.1.1 Materials

The samples were fabricated by coating two commercial GDLs with in-house prepared MPLs and CLs, before hot-pressing around a PA-doped commercial PBI membrane. The GDL used

was a 280-µm-thick carbon paper (TGPH 090, Toray) containing 5 wt% polytetrafluoroethylene (PTFE). The MPL ink constituted 90 wt% Ketjen black (EC-300J, AkzoNobel) and 10 wt% PTFE (Sigma Aldrich) in iso-propanol (IPA), giving a Ketjen black MPL loading of 1 mg.cm^{-2}. The CL ink was prepared by blending 80 wt% Pt/C catalyst (60% Pt loading, Fisher Scientific) and 20 wt% PTFE in a 2:3 mixture of de-ionized water and IPA. The 30-µm-thick PBI membrane (Fumapem® AP-30, Fumatech) was doped with PA by immersing in 85 wt% orthophosphoric acid (PA, Fisher Scientific) at 140 °C for 6 h. The doped membranes were vacuum-dried at 80 °C for 3 h to remove moisture and calculate the acid doping level (ADL). The ADL was calculated according to Equation 1.

Equation 1:

$$ADL = \frac{W_{PA}}{M_{PA}} / \frac{W_{PBI}}{M_{PBI}}$$

where W_{PA} and W_{PBI} are the wt% content of PA and PBI, respectively, and M_{PA} and M_{PBI} are the molar mass of PA and the polymer repeat unit, respectively. For all membranes, the ADL was approximately 11.5, representative of other literature preparations[9][10][11].

2.1.2 Assembly

The MPL was spray-coated onto each GDL using nitrogen, and the solvent removed by heating at 120 °C for 10 s between each coat, after which each MPL-coated GDL was sintered at 300 °C for 3 h. Subsequently, the CL ink was sprayed on the MPL, and the solvent similarly removed, giving a final CL loading of 1 mg$_{Pt}$.cm^{-2}. The samples were assembled by sandwiching the membrane between GDEs, using 150-µm-thick PTFE gaskets, hot-pressing the assembly at 140 °C for 270 s, with a constant pressure of 80 psi. The electrodes were square with an active area of 225 mm^2 in all cases.

2.1.3 °Electrochemical methods

The hot-pressed samples were assembled into a single-cell 4 x 4 cm^2 test rig, designed in-house, compressed with 0.5 N.m torque and operated at 150 °C. Polarisation curves were collected, and electrochemical impedance spectroscopy (EIS) was performed for Sample Sets A and B, with the addition of cyclic voltammetry (CV) for Sample Set B. Using a potentiostat (E5000, Gamry), polarisation curves and EIS measurements were collected with

100 mL.min^{-1} of dry hydrogen on the anode and dry oxygen on the cathode, and CV used 33.4 mL.min^{-1} dry hydrogen on the anode and 140 mL.min^{-1} dry nitrogen on the cathode. The cathode of each MEA served as the working electrode, where the anode served as the counter and reference electrode in a typical 2-electrode set-up.

Once the open-circuit voltage (OCV) stabilised, ten polarisation curves were collected by discharging from OCV to 0.1 V in 0.1 A steps with 5 s dwell time, and the final polarisation curve taken as the steady-state condition. Galvanostatic EIS was performed at 0.5 A (0.22 A.cm^{-2}) across a frequency range of 10,000 to 0.1 Hz, with a perturbation current of 10 mA. CV was performed between 0.05 and 0.5 V with a scan rate of 100 mV.s^{-1} and the hydrogen desorption curve used to calculate the electrochemical surface area (ECSA) of the catalyst on the working electrode side using Equation 2.

Equation 2:

$$\mathrm{ECSA}(cm^2{}_{Pt}/g_{Pt}) = \mathrm{Charge}(\mu C.cm^{-2})/[210(\mu C.cm^{-2}{}_{Pt}) \times \mathrm{Catalyst\ Loading}(g_{Pt}.cm^{-2})$$

Sample Set A underwent lifetime testing by running each cell at constant current, at the value associated with an initial voltage of ~0.6 V, for up to 100 h. A single cell was characterised immediately after hot-pressing, again after 50 h of operation, and finally after having operated for 100 h in total. X-ray CT characterisation was carried out for identically fabricated cells after 0, 50 and 100 h of operation. Sample Set B underwent accelerated stress testing (AST) which consisted of repeated chronopotentiometry – 4-minute operation at 0.6 A.cm^{-2} followed by 16-minute operation at 1.0 A.cm^{-2}, for a total of 6 h[35]. The cells were held at OCV for ten minutes between each cycle, and the cycle repeated a total of 11 times, such that the entire testing regime lasted approximately 70 h. X-ray CT characterisation was carried out on identically prepared pristine samples and the AST samples.

2.2 X-ray micro-CT

2.2.1 Sample preparation

A laser micro-machining tool (A Series/Compact System, Oxford Lasers) was used to mill multiple circular discs of either 1.5 or 2 mm from the active area at ~0.8 W and at a scan speed of ~ 1 mm s^{-1}, and 2-3 iterations. This size was chosen as a balance between improved

signal-to-noise for a given exposure time and the need for a representative volume[38][39]. To ensure laser milling did not affect the sample discs more than mechanical cleavage, similar half-cell samples were prepared; a laser-milled and a mechanically hole-punched disc, each 1.5 mm in diameter, both immersed in 85 wt% PA at room temperature for 10 s. Volume renderings and XZ-orthoslices are shown in **Error! Reference source not found.** for comparison, illustrating that the delicate microstructure is in fact more deformed by mechanical cleavage than by laser micro-machining. Sub-volumes (0.16 mm^3) from the two GDLs gave similar porosities (54% and 49% for mechanical and laser, respectively), indicating a similar PA content in both.

To improve the statistical robustness of the resulting tomographic analysis, a procedure for scanning multiple subsamples from each sample MEA was developed. An in-house sample holder (jig), compatible with the X-ray CT instrument's sample stage, was designed in SolidWorks (Dassault Systèmes), 3D-printed using a Form 3 (Formlabs) 3D printer, and each disc was individually placed into the recess of one jig part, before building into a stack and securing within the X-ray CT sample holder chuck. For Sample Set A, the samples were cut out completely before being placed in jig parts; in the process, the 'anode side' and 'cathode side' information for the operated samples was lost. However, for Sample Set B, two rather than three iterations of milling were used to leave the discs just intact such that each could be gently coaxed into the recess from the bulk MEA, retaining the 'anode side' facing upwards for all samples. CAD and optical images of the 3D-printed jig are shown in **Error! Reference source not found.**. The advantage of this design is that acquisition for multiple samples (5-10) can be set up all at once in a multi-recipe scan, utilising overnight periods, despite scan times of only 2-4 hours per sample.

2.2.2 Image Acquisition

An X-ray micro-CT instrument (Zeiss Xradia 520 Versa, Carl Zeiss) was used for all scanning in this study, equipped with a polychromatic source with a tube voltage range of 30-160 kV. A 4× objective was chosen to give ~1 µm voxel dimension with a ca. 2 mm field-of-view at reasonable source-to-sample and sample-to-detector distances. Preliminary scanning was

conducted to evaluate the degree to which PA could be discerned from other materials, hence "half cells" (GDL/MPL/CL) were fabricated and scanned both "dry" (pristine) and "wet" (85 wt% PA).

Figure 1a shows two-dimensional slices (orthoslices) from X-ray CT tomograms of half-cells imaged in "dry" and "wet" (laser-milled disc shown in **Error! Reference source not found.**) states. Previously, synchrotron tomographic imaging with a monochromatic 20 kV beam was shown to give distinguishable peaks for carbon fibres and binder in dry samples, but not in wet samples saturated with low concentration PA[24].

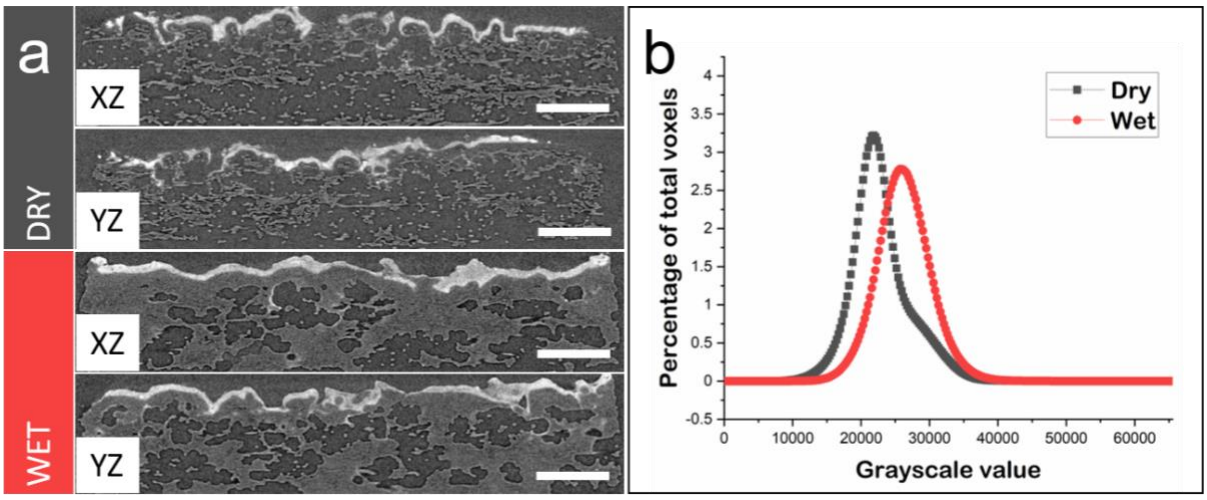

Figure 1: a) XZ- and YZ-orthoslices of dry and wet "half-cells" comprising GDL, MPL and CL. b) Histogram comparison between sub-volumes taken from the GDL of each volume. All scalebars denote 200 µm.

Figure 1b shows a similar trend is observed where a higher grayscale shoulder in the dry sample is obscured in the wet sample where the presence of PA effectively renders the fibres, binder and PA one phase. It should be noted that this is the case even at relatively high PA concentration (~85 wt%) as here a lab-based polychromatic X-ray beam with a peak energy of 80 kV (as used in previous studies[35],[40]) has been used. Lower peak energies were selected for further scanning, a trade-off between improving contrast and retaining adequate flux for sufficient signal-to-noise ratio. X-ray acquisition parameters used in this study are shown in **Error! Reference source not found.**, the key differences being highlighted in Table 1.

Table 1: Key X-ray CT acquisition parameters used in this study.

Sample Set	X-ray voltage (kV)	Voxel size (µm)	Exposure time (s)	Projection Number	Scan time per sample (h)

Half-cells	80	1.09	8	801	1.8
A	60	0.95	14	1101	4.3
B (Pristine)	40	1.01	25	401	2.8
B (AST)	50	1.01	25	501	3.5

For Sample Set A, the X-ray parameters were internally consistent, but the X-ray energy was lowered between the sets to improve contrast and consequently, the exposure time was increased to retain good signal-to-noise. The Sample Set B pristine (0 h) samples were scanned with a low energy of 40 kV and minimal projections, both of which were increased slightly for AST samples to improve data quality, retaining the same voxel dimension. Generally, the number of projections was lowered versus the half-cell scans to facilitate shorter scans, whilst retaining adequate image quality. Slightly larger diameter discs (2.0 versus 1.5 mm) were used to ensure that all replicates had the “anode side” facing upwards as this was practically more difficult with smaller discs. Therefore, the optimised parameters allow for seven to eight scans of 2-mm-diameter HT-PEFC discs with sufficient data quality for segmentation, within a 24 h period.

2.2.3 Data Processing

Each set of collected radiographs was reconstructed using a proprietary version of the Feldkamp-Davis-Kress (FDK) cone-beam algorithm[41] in XMReconstructor (Carl Zeiss). Each tomogram was processed in the same way to minimise variation: the data was transformed to be planar and cropped to produce cuboidal volumes. 3D renderings of these tomograms are shown in Figure 2. From the series of tomograms comprising each sample set, the largest cuboidal sub-volume was extracted that avoided the inclusion of air external to the cylindrical sample; for Sample Set A this was 1070 × 1070 × 525 voxels (0.533 mm^3), for Sample Set B this was either 1013 × 1013 × 507 voxels (Pristine) or 1015 × 1015 × 508 voxels (AST) (both also 0.533 mm^3). XZ- orthoslices from each of the subvolume tomograms from Sample Set A and Sample Set B are shown in **Error! Reference source not found.** and **Error! Reference source not found.**, respectively. Each tomogram was filtered twice, first with a 3D non-local means filter (search window=10 pixels; local neighbourhood=3 pixels)

which dramatically reduced the noise. Secondly, to enhance the feature edges, a 3D unsharp masking filter (edge size=9 pixels; edge contrast=0.9) was applied.

To perform segmentations in a robust and time-efficient manner, particularly given the high number of tomograms involved, segmentation was performed using a two-stage, semi-automated approach, harnessing the power of machine-learning based segmentation (using freeware, Ilastik[42]) to perform the majority of voxel allocation, combined with a localised approach (performed in Avizo[43]) for membrane identification, phase separation and final adjustments. In the first stage, the machine-learning step achieves a ternary segmentation: high grayscale is allocated to the CL, low grayscale is allocated to Pore, and intermediate grayscales are allocated to a combined GDL/MPL/Membrane (and PA where applicable) phase. Subsequently, a localised procedure is used to segment Membrane from the other phases, as it is indistinguishable in grayscale value at 40-60 keV, and the resultant segmented volume was further divided into anode and cathode sides for Sample Set B, with *a priori* knowledge. An example of raw, filtered and segmented orthoslices from a single Sample Set A tomogram is shown in **Error! Reference source not found.**.

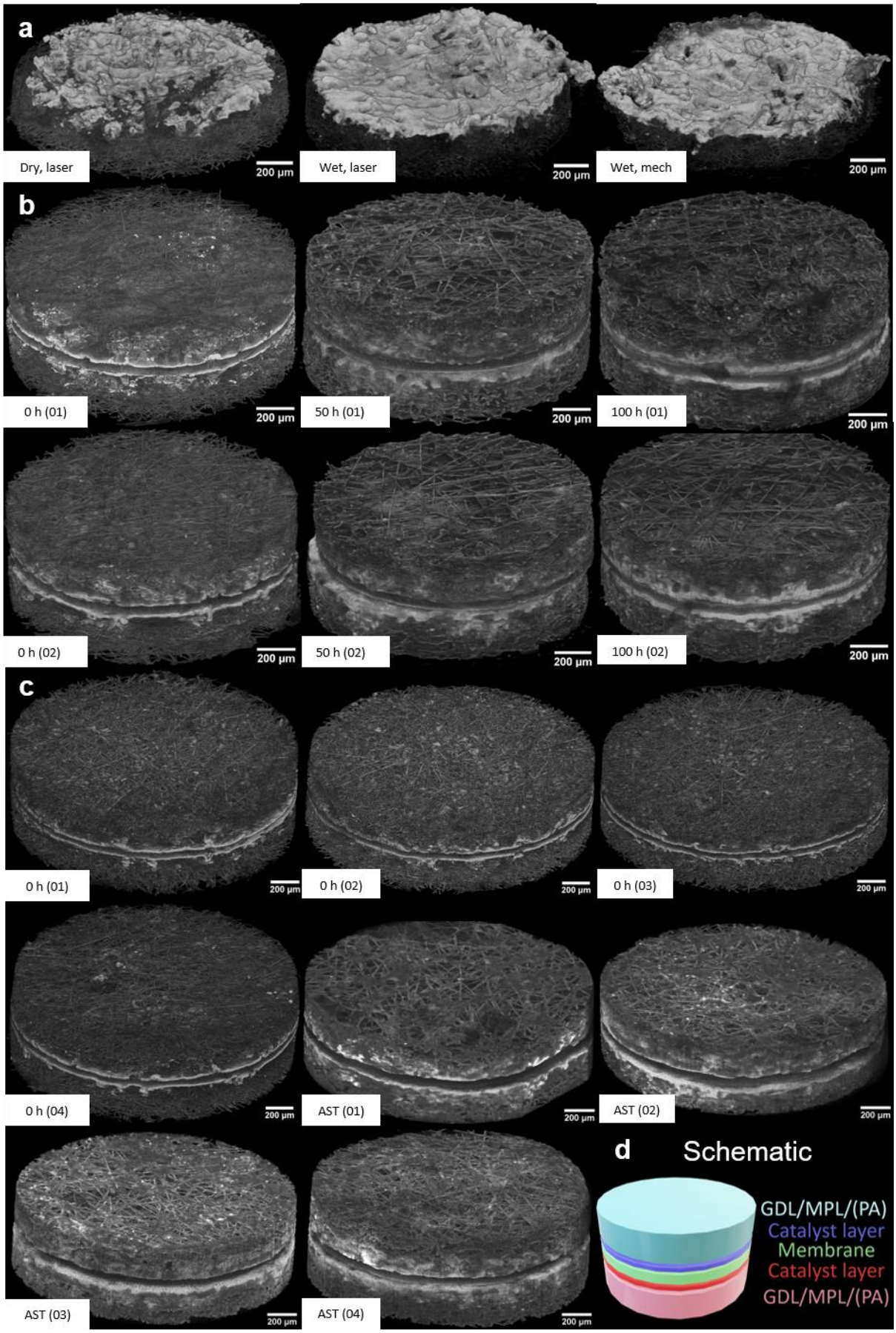

Figure 2: Volume renderings of processed tomograms from a) half-cell tests and b) lifetime tests on Sample Set A; c) AST tests on Sample Set B; d) Schematic illustrating the different layers of all samples.

The processed volumes are imported into Ilastik as 2D TIFF stacks, selecting all pre-defined "features" (convolutional kernels)[42], and performing an initial user training by manually "painting" a small portion of the central slice in the *XZ*-direction. An initial machine-learning segmentation is computed and displayed, which allows the user to interact with the result to suggest further refinements before an updated segmentation is proposed. The initial training input, initial suggested segmentation, additional training and updated segmentation for the same central slice of a single tomogram is shown in **Error! Reference source not found.** as an illustration. Additional interaction by the user can be carried out on additional slices any orientation, specifically targeting areas of high uncertainty and regions that appear under or over-segmented from the first pass. For Sample Set A, training was undertaken on the central *XZ*-slice (20 min), and additions were made on the same slice (20 min) and a slice in the other directions (10 mins each) to give a result within one hour of interacting with the data. For Sample Set B, despite lower signal-to-noise ratio, only 30 min was required to provide a similarly visually acceptable segmentation.

Stage two consisted of importing the output from Ilastik, along with the raw image, into Avizo and manually segmenting the membrane from the GDL, since the membrane is spatially separate from the other features but possesses similar grayscale. This segmentation was achieved by first using the outer edge of the pre-segmented CL to create a "Mask" phase. The combination of this phase and CL acted as an effective barrier, such that voxels with the grayscale values selected for segmentation using the "Magic Wand" tool would remain within the boundary of the "Mask+CL" region. The "Magic Wand" was used to select many narrow grayscale regions, which slowly built up the membrane phase. Finally, interpolation between slices, in either the *xz*- or *yz*-planes, was performed to fill any gaps, and the final segmentation was manually adjusted to smooth the membrane edges. Attempting a quaternary segmentation with the machine-learning approach proved problematic, leading to an under- or over-segmentation of GDL. Once this two-stage segmentation was complete, the two sides of the membrane were labelled separately, and final adjustments made to amend any major residual misallocations by manual re-allocation.

2.2.4 Data Analysis

Phase fraction calculations were computed in Avizo by simple voxel counting, and represent a proportion of the total volume, unless otherwise stated. The phase fraction for unoperated samples represents the carbonaceous phases that constitute the GDL and MPL, whereas the analogous phase fraction for operated samples represents these phases plus migrated PA. Clear distinction of PA from the carbonaceous phases was not possible with a polychromatic (40-60 keV) X-ray beam, and comparisons were drawn across samples, both for bulk and slice-by-slice analysis. It is worth noting that no lab-based system has yet shown sufficient contrast for direct segmentation and instead, complex *operando* set-ups have been required in order to subtract "dry" from "wet" images[27][44]. Here, we leverage the multi-sample, high-throughput procedure to provide statistically more robust estimates of PA distribution as a function of fuel cell operation. Volume-specific surface areas (VSSA) are calculated by producing surfaces from the voxel reconstructions and dividing the summated area by the total volume of that specific phase.

To probe PA penetration into the GDL, a slice-by-slice (*Z*-direction) analysis was undertaken for all volumes. As PA penetrated deep into the GDL, and to avoid the uncertainty caused by variations in MPL phase fraction, the first and last 150 slices were also used to calculate average phase fractions for pore and GDL(/PA) for comparisons between unoperated and operated cells in the "strictly GDL region". Measurements of membrane thicknesses were performed by taking the full-width at half-maximum (FWHM) approach to the central peak, and inter-CL distances were peak-to-peak maxima distances. To characterise the pore domain, tortuosity factor in the *z*-direction (τ_z) and continuous pore size distributions (cPSD) calculations were performed in TauFactor[45] and ImageJ, respectively. Tortuosity factor (τ) in this formulation is defined in Equation 3:

Equation 3:

$$D^{eff} = D\,\frac{\varepsilon}{\tau}$$

Where ε is the porosity in this study, D is the intrinsic diffusivity of whichever gas is flowing in the pores, and D^{eff} is the effective diffusivity given by the presence of the solid phase. cPSD

calculations follow an algorithm developed by Münch *et al.* that involves the determination of the amount of pore volume that can be filled with spheres of given radius, characterising a continuous pore volume as if it were composed of a distribution of these spheres. The reader is referred to [46] for more detail and a mathematical description of the algorithm.

Given both the greater solid density in the MPL region and its almost complete filling in operated samples, GDL regions were selected by choosing an appropriate slice number from the slice-by-slice analysis of each dataset. For the pristine samples, this value was taken at the elbow-point of the CL, where there was a noticeable change in CL "area", typically ~200 slices. For the aged samples, because of the greater intrusion of the PA into the pores, values were chosen where the GDL/MPL (PA) phase fraction equalled the pore phase, typically ~150 slices. This ensured that the complete flooding of pores near the CL did not distort the values for pore size and tortuosity of the GDL/MPL. Importantly, attempts to quantify τ_z through entire GDEs often gave very high or even infinite values due to low or no percolation at the imaged resolution such that focus was given to residual percolated volumes after PA leaching. After extraction of the subvolumes from both the top and bottom of each sample, the datasets were binarized to form "solid" and "pore" phases, before application of the tortuosity factor and cPSD procedures. Where "± errors" are reported, the standard error of the mean is given, equivalent to the sample standard deviation divided by the square root of the number of measurements made.

3 Results and Discussion

3.1 Sample Set A

100 h of operation at constant current was monitored by taking voltage readings throughout, measuring polarisation curves at 0, 50 and 100 h, and performing EIS before and after operation (Figure 3). Figure 3a clearly shows that operating at a fixed current density is accompanied by significant degradation (20 mV between 20 h and 100 h) within a relatively short duration, which is equivalent to 10% voltage loss in less than 250 h (where the current US DoE target is 5000 h[47]). This early-stage degradation corresponds to a loss of ca. 200 $\mu V.h^{-1}$ which is an order of magnitude greater than previous durability studies[48][49]. This

may be because the cell in this work is considerably smaller than those examined in the literature such that detrimental edge effects may be enhanced. Additionally, the tests presented here are shorter term (100 h versus 800-1000 h in the literature), such that a plateau in voltage after 100 h would imply an over-estimation of degradation. Finally, and potentially most importantly, the doping procedure (85 wt% orthophosphoric acid at 140 °C for 6 h) and level (ADL = 11.5) were specifically chosen to exacerbate PA leaching for electrochemical and microstructural analysis, rather than using a polyphosphoric route[48] shown to give improved physicochemical properties[50] or a lower doping level (e.g. ADL = 3.5[49]). The polarisation curves display the same trend, with maximum current densities of 407 mW.cm^{-2} at 0 h, 390 mW.cm^{-2} at 50 h and 365 mW.cm^{-2} at 100 h (average -0.4 mW cm^{-2} h^{-1}). The complex plane plot in Figure 3c illustrates that the ohmic contribution to impedance is approximately unaffected by operation, but that there is an appreciable increase from 0.31 to 0.35 Ω.cm^2 (~13%) in the sum of charge transfer resistance and mass transfer resistance, also evident at low and high current densities, respectively, in the polarisation curves shown in Figure 3b. Attributing losses specifically to either or both of the anode and cathode is beyond the scope of this work.

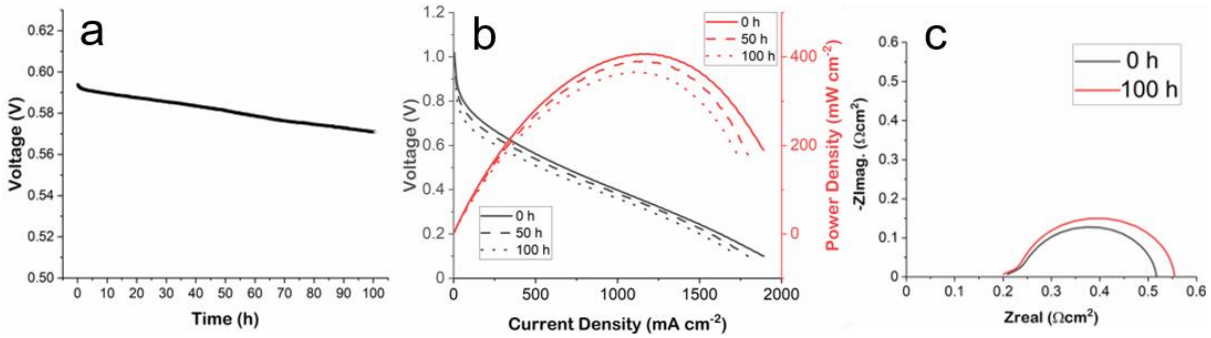

Figure 3: Electrochemical data pertaining to Sample Set A, a) Voltage-time plot for the duration of operation; b) Polarisation curves (black) and power density curves (red) for 0 h (line), 50 h (dashed) and 100 h (dotted); c) Complex plane plots for 0 and 100 h.

A single *XZ*-orthoslice from filtered and segmented tomograms for each sample is shown in Figure 4. The defined fibrous structure of the GDL is evident in both 0-h-samples (Figure 4 a,c), attributable to a lack of observable PA in any of the micron-sized pores. Although hot-pressing can lead to a small quantity of PA escaping the MEA, the porous microstructure of the GDL-MPL layers is still visibly empty. This is not the case in either the 50- or 100-h-

samples, where significant quantities of PA have migrated into the porous microstructure, in both cases partially but appreciably filling the MPL and GDL layers.

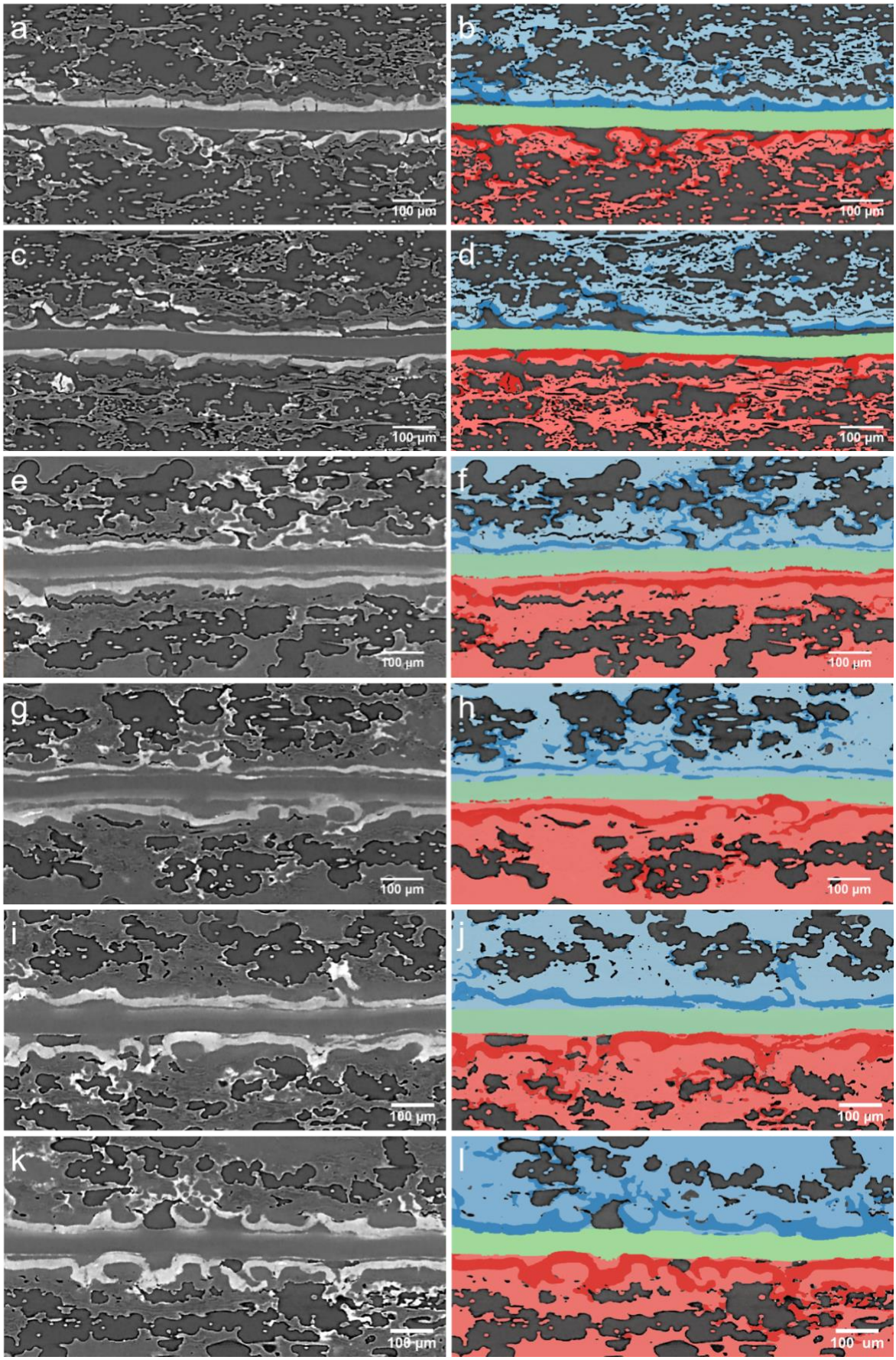

Figure 4: X-ray CT data pertaining to Sample Set A: Filtered XZ-orthoslices from a), c) 0 h tomograms; e), g) 50 h tomograms; i), k) 100 h tomograms; Corresponding segmented XZ-orthoslices from b, d) 0 h tomograms; f, h) 50 h tomograms; j, l) 100 h tomograms.

From the segmented datasets, phase fractions are calculated for seven phases - three phases for top and bottom (CL, Pore, and combined GDL-MPL – and PA where applicable) plus the membrane. PA cannot be reliably segmented from the GDL, but bulk phase fractions from operated and unoperated samples, shown in Table 2 and **Error! Reference source not found.**, provide an estimate of the leached PA, with the full global phase fraction results shown in Table S2. In 0-h-samples, the GDL/MPL phase accounts for 14-15% of the total volume, consistent for both sides and samples, providing a baseline against which to compare operated samples. Notably, the VSSA was 0.33 & 0.31 μm^{-1} and 0.34 & 0.33 μm^{-1} for the top & bottom of 0 h (01) and 0 h (02), respectively; this high level of similarity representing successful segmentation that captures the same morphology of material, regardless of side or sample. In both the 50-h-samples and 100-h-samples, there is a significant increase in this phase fraction, due to PA leaching. For 50-h-samples, the average GDL/MPL/PA phase fraction increases to 24% and 28% for the top and bottom, respectively, which represents an average sample increase of 11.2 ± 1.6% by volume (~0.06 mm^3 in absolute terms) at one electrode. Similarly, for 100-h-samples, the same phase fraction shows an increment of 10.0 ± 2.4% by volume (~0.05 mm^3) versus 0-h-samples, although there is greater variation in the replicates compared with the 50-h-case (26% and 24% versus 26% and 26% for the 100-h- and 50-h-cases, respectively). The results of an analysis of the first and last 150 slices (GDL only) are shown in **Error! Reference source not found.**. The average phase fraction when excluding the MPL region increases from 0.30 (0 h) to 0.55 (50 and 100 h), equating to a concomitant filling of ~35% and 40% for 50 h and 100 h (due to a small difference in CL distribution). Both the full electrode and GDL-only analysis imply that between 0 and 50 h, a substantial amount of PA egresses from the membrane and CL into the pore space of the GDL/MPL, consistent with literature that suggests GDL flooding reaches a steady-state in just a few hours[25]. Although this quantity does not increase substantially in the following 50 h, the data suggests an increasing heterogeneity in PA distribution with time, such that the impact of longer-term testing on PA distribution requires further investigation.

Table 2: Global GDL/MPL/(PA) phase fraction for each sample and comparisons versus the pristine state.

Electrode	GDL/MPL/(PA) Phase fraction				
	0 h Mean	50 h Mean	100 h Mean	50 h vs 0h	100 h vs 0h
Top	15.3%	23.7%	28.7%	8.4%	13.4%
Bottom	14.0%	28.0%	20.6%	14.0%	6.7%
Mean	14.6 ± 0.4%	25.8 ± 1.5%	24.7 ± 2.4%	11.2 ± 1.6%	10.0% ± 2.4%

To inspect the degree of PA egress, slice-by-slice analysis was conducted (Figure 5), plotting each phase's area fraction from the bottom (Layer 1) to the top (Layer 535). Note that each layer is ~0.95 µm thick. First, it is observed that the membrane thickness (FWHM) increases a little with operation time, from ~45-48 µm (0 h, Figure 5 a,b), to ~49-51 µm (50 h, Figure 5 c,d), to ~52-56 µm (100 h, Figure 5 e,f), although these small increments with only duplicate data require further investigation to confirm. The CL areal fraction peak tends to move further from the membrane with operation time, and an increased overall magnitude and greater magnitude in each curve's "tail" is observed, depicting increasing penetration of Pt into the GDL with operation. Of course, there is no physical reason to suspect that the true quantity of Pt increases as a function of operating time; instead, the bulk phase fraction increase is an artefact of the fact that even small quantities of very electron-dense Pt appear appreciably bright in the tomograms to be allocated as such. Thus, Pt migration that is not complete but involves migratory and residual metal yields an effective increase in measured CL phase fraction. It is also observed that the CL peaks after 100 h are taller and narrower, suggestive of inner Pt that is close to the membrane migrating outwards to amass at the newly established interface, as well as Pt migration into the GDE, although this requires more experimentation to confirm. Overall, the observed Pt migration may explain the greater activation losses seen in the operated cells' polarisation curves in Figure 3b. Membrane thickness and inter-CL distance data are given in **Error! Reference source not found.**.

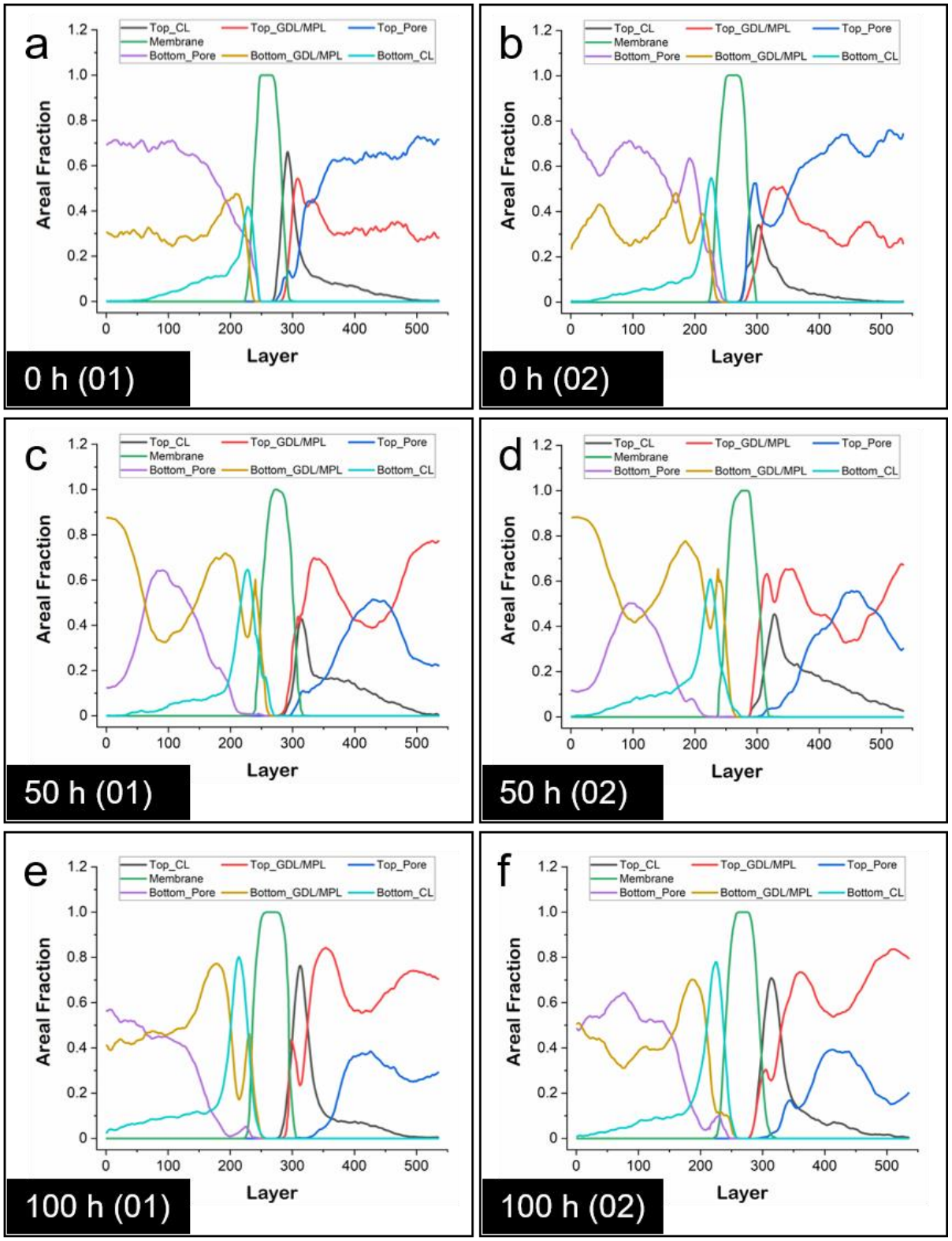

Figure 5: Slice-by-slice plots for Sample Set A, showing the area fraction for each of the seven phases from the bottom (Layer 1) to the top (Layer 535) for (a) 0 h (01); (b) 0 h (02); (c) 50 h (01); (d) 50 h (02); (e) 100 h (01); (f) 100 h (02).

Importantly, the curves pertaining to the GDL/MPL phase (0 h, Figure 5a,b)) and GDL/MPL/PA composite phase (50 h, Figure 5c,d and 100 h, Figure 5e,f) present different shapes. In Figure 5a,b, there are peaks for both sides attributable to the MPL region, followed

by an average of ~30% carbonaceous volume. However, in Figure 5c,d, there are broader and higher peaks just after the MPL, *and* secondary, taller peaks towards the top and bottom of the GDL (where the flow-fields had been). In this case, from GDL-only calculations, the average GDL/MPL/PA phase fraction is ~55%. Despite very similar values in bulk quantity in 100-h-samples (also ~55%), the distribution can be seen (Figure 5e,f) to differ, versus 50-h-samples (Figure 5c,d). In the 100-h-case, one of the sides retains the double peak, whereas the other has a much less significant peak towards the flow-field end and there is a large discrepancy between the amount of PA on both sides. As this analysis only captures the residual PA inside the GDL/MPL, further work to inspect the volume of PA that escapes *via* the flow-field is planned using an *in-situ* set-up.

The impact on the porous network was investigated by both cPSD and tortuosity factor measurements for each GDL layer of all six samples. The cPSD results are summarised in Table 3. There is little difference in the average (r_{50}) pore sizes between the two sides of the unoperated MEAs. For 50-h-samples this remains the same with a small increase in intrasample difference for 100-h-samples. However, there is a significant measured difference in pore r_{50} between the unoperated cells (12.6 ± 0.2 µm) and operated cells (15.5 ± 0.2 µm and 15.7 ± 0.4 µm for 50 h and 100 h, respectively). These changes represent average increases of 23% and 25% for 50 h and 100 h, respectively. Given the inundation of the GDL with PA, and the greater mass transport losses seen in Figure 3, it might appear counterintuitive that the average pore size increases for the operated cells. However, there is a wide PSD for the unoperated cells, including many small pores that are mainly filled in the operated cases, causing the median value to increase. Moreover, it is not just the pore size that is important, but also the connectivity and “constrictivity” of the pore throats that must be considered. It is also worth noting that although the solid phase r_{50} values for the “dry” fibres for both sides of both 0-h-samples are very similar (4.4-4.7 µm), much greater magnitude and variation is observed for both operated samples due to the inclusion of PA in the solid phase and its uneven distribution across the two sides of the membrane.

Table 3: Summary of Pore cPSD results for Sample Set A

Sample	Electrode	Pore r_{50} (µm)	Mean Pore r_{50} (µm)	Top/Bot. Pore r_{50} (µm)
0 h (01)	**Top**	12.2	12.4	0.98
	Bottom	12.5		
0 h (02)	**Top**	13.2	12.8	1.06
	Bottom	12.4		
0 h Mean	**Top**	12.7	12.6 ± 0.2	1.02
	Bottom	12.4		
50 h (01)	**Top**	14.9	15.2	0.97
	Bottom	15.4		
50 h (02)	**Top**	15.4	15.7	0.96
	Bottom	16.1		
50 h Mean	**Top**	15.2	15.5 ± 0.2	0.97
	Bottom	15.7		
100 h (01)	**Top**	16.2	15.4	1.11
	Bottom	14.6		
100 h (02)	**Top**	15.5	16.0	0.93
	Bottom	16.6		
100 h Mean	**Top**	15.8	15.7 ± 0.4	1.01
	Bottom	15.6		

The *z*-tortuosity factor (through-plane) results of the binarized GDL volumes are shown in Table 4. Despite the increasing r_{50} upon operation, there is a significant increase in tortuosity factor from 4.5 ± 0.8 in 0-h-samples to 10.6 ± 3.2 in 50-h-samples. The mean pore τ_z of 100-h-samples is also greater than in the unoperated cells but there is a significant difference between each GDL per sample.

Table 4: Summary of z-tortuosity factor (τ_z) results for Sample Set A

Sample	Electrode	Pore τ_z	Connectivity	Mean Pore τ_z	Top/Bot. Pore τ_z
0 h (01)	**Top**	4.33	99.7%	4.0	1.20
	Bottom	3.61	99.7%		
0 h (02)	**Top**	4.42	99.6%	5.0	0.81
	Bottom	5.49	99.8%		
0 h Mean	**Top**	4.38	99.7%	4.5 ± 0.4	0.96
	Bottom	4.55	99.8%		
50 h (01)	**Top**	11.2	95.7%	10.7	1.10
	Bottom	10.2	97.0%		
50 h (02)	**Top**	6.53	95.6%	10.4	0.46
	Bottom	14.3	95.9%		
50 h Mean	**Top**	8.87	95.7%	10.6 ± 1.6	0.72
	Bottom	12.3	96.5%		
100 h (01)	**Top**	9.34	88.0%	7.2	1.86
	Bottom	5.02	96.8%		
100 h (02)	**Top**	11.5	88.8%	7.2	3.90
	Bottom	2.95	98.6%		
100 h Mean	**Top**	10.4	88.4%	7.2 ± 2.0	2.61
	Bottom	3.99	97.8%		

Although the pore τ_z is approximately equal for both sides of both 0-h-samples, the variance in this value increases with operation time. The pore network in the 50 h (01) sample appears to have been uniformly hindered with PA distributed similarly on both sides, but despite a

similar connectivity, the 50 h (02) sample is more severely affected by PA in the bottom electrode than the top. In 100-h-samples, there is an even larger discrepancy in the pore τ_z on either side of the membrane, and in this case, this is matched by a concomitant drop in connectivity. The increased resistance to gas permeation between the current collector side and the membrane side in one GDL of each of the 100-h-samples correlates with the increase in mass transport polarisation losses shown in Figure 3c.

3.2 Sample Set B

To improve the statistical significance of the data collected, and by using a standard AST available in the recent literature[35], a second set of samples was investigated in quadruplicate. Electrochemical testing was performed both on the pristine cell (0 h) and after the 70-h of load cycling between 0.6 and 1.0 $A.cm^{-2}$ of the same. Voltage readings were taken throughout, as well as measuring pre- (0 h) and post- (AST) polarisation curves, along with EIS and CV curves, shown in Figure 6. XCT samples were taken from the AST sample and compared with a separate 0 h sample made following the same procedure and material batch.

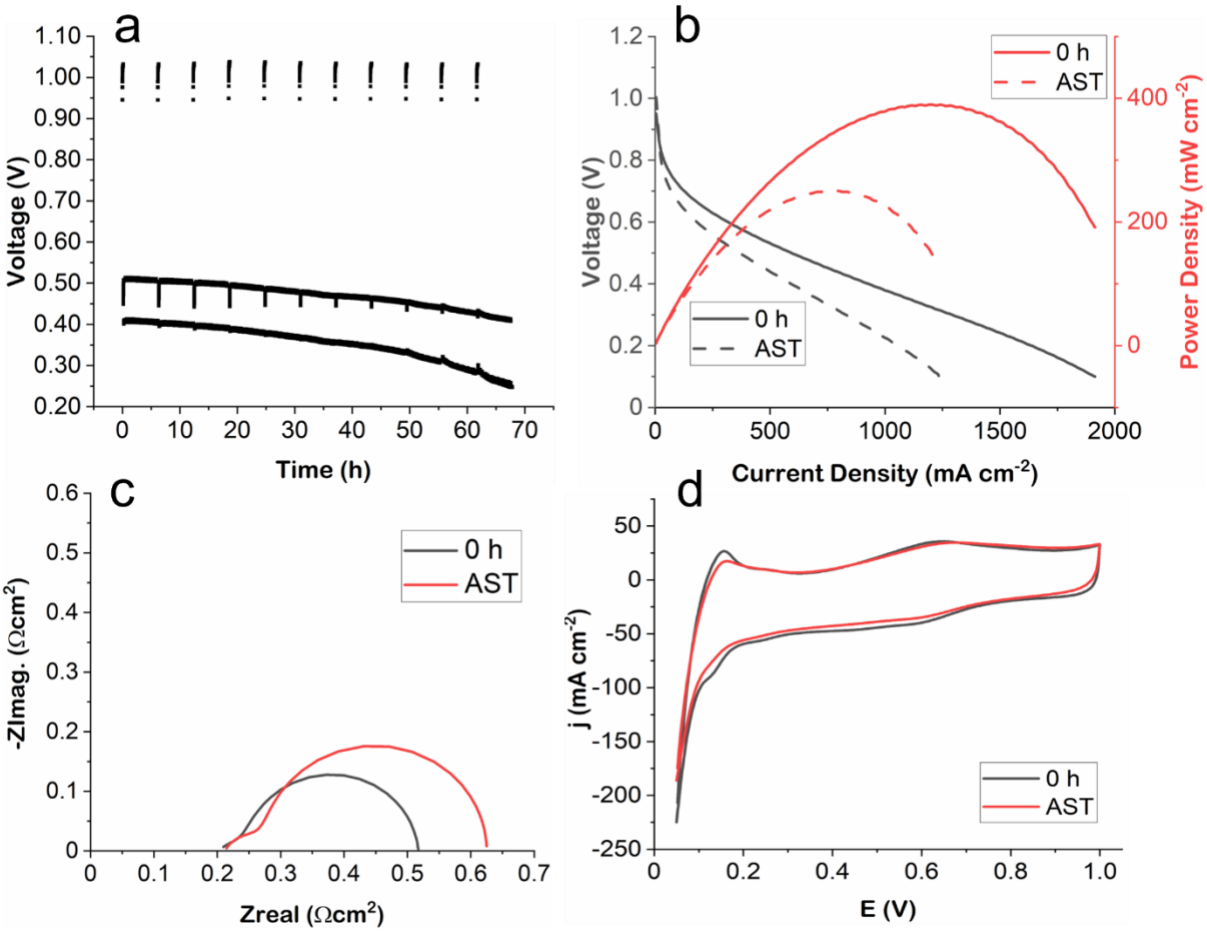

Figure 6: Electrochemical data pertaining to Sample Set B, a) Voltage-time plot for the duration of operation; b) Polarisation curves (black) and power density curves (red) for 0 h (line) and AST (dashed); c) complex plane plot for before (black) and after (red) AST; d) Cyclic voltammograms for before (black) and after (red) AST.

A significant decline in performance is clearly observable in the voltage drop seen at either current density (Figure 6a), 10 mV at 0.6 A.cm^{-2} and 16 mV at 1.0 A.cm^{-2} over ~70 h, similar in magnitude to the voltage drops observed in Sample Set A. All three 'regimes' in the polarisation curves (Figure 6b) and in the magnitude of the semi-circular arcs in the complex plane plot (Figure 6c) also signal significant performance degradation. The greater activation and mass transport losses seen in the polarisation curve are reflected in the emergence of an observable mid-frequency arc in the complex plane plot and an increase from 0.31 to 0.41 Ω.cm^2 in overall polarisation resistance (~32% increase). There is minimal increase in the DC ohmic resistance (high-frequency intercept), which is thought to be due to more than sufficient PA doping in PBI such that a certain degree of PA leaching does not have a significant impact on the conductivity of the membrane. However, an ohmic loss increase is more apparent in the polarisation curve. This may be due to acid leaching and catalyst

migration causing the dead region between catalyst layer and membrane to become larger, whilst the membrane resistance is only minimally impacted.

The CV curves shown in Figure 6d illustrate a small drop in ECSA, measured to be 55.4 $cm^2.mg^{-1}$ in the 0 h cell and 50.0 $cm^2.mg^{-1}$ in the AST cell, representing a ~10% decrease, accounting for increased activation losses. The sum of charge transfer resistance and mass transfer resistance in the pristine cell is 0.29 $\Omega.cm^2$, very similar to that seen for Sample Set A (0.31 $\Omega.cm^2$), which increases to 0.38 $\Omega.cm^2$ after the AST, representing a ~31% increase. The membrane swelling, Pt migration and PA egress from the membrane (Figure 7) qualitatively capture the correlation of microstructural change with these indicators of electrochemical performance decline. However, the degradation effects observed here are likely compound effects arising from multiple, independent degradation mechanisms. Unlike LT-PEFCs, which have established ASTs to target specific modes of degradation, HT-PEFCs still lack standardised AST protocols. Thus, future work should aim to develop such targeted ASTs, which would allow for direct correlation between electrochemical degradation and morphological changes in the MEA components observed by X-ray CT.

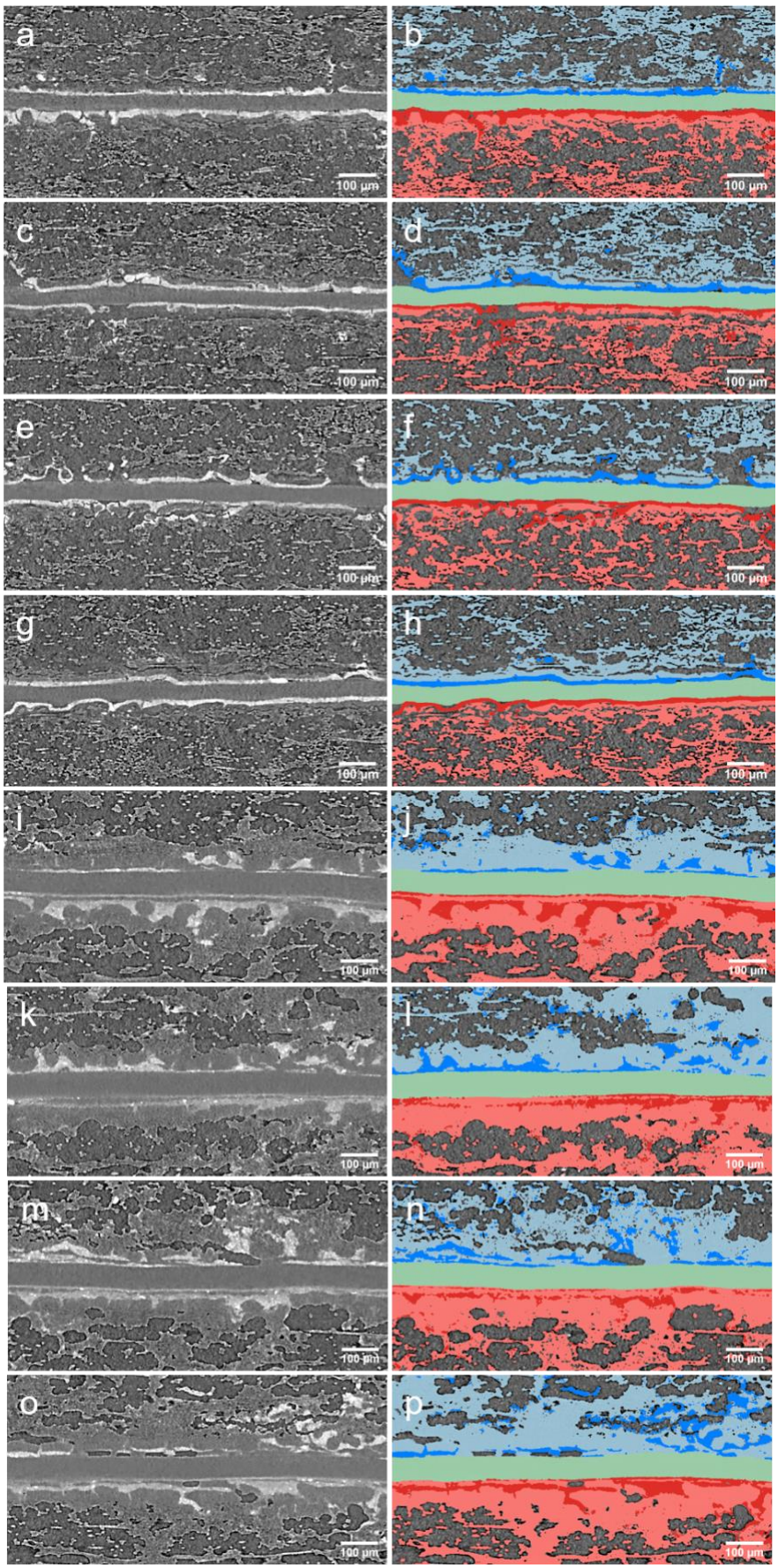

Figure 7: X-ray CT data pertaining to Sample Set B: Filtered XZ-orthoslices from a), c), e), g) 0 h tomograms; b), d), f), h) Corresponding segmented XZ-orthoslices from 0 h tomograms and from i), k), m), o) AST tomograms; j), l), n), p) Corresponding segmented XZ-orthoslices from AST tomograms.

The segmented volumes were analysed quantitatively, both globally and by a slice-by-slice method. The full results from this analysis are given in **Error! Reference source not found.** and a summary of the GDL/MPL (unoperated) and GDL/MPL/PA (operated) composite phase fractions are shown in Table 5. Importantly, the average phase fraction for the PA-free carbonaceous phase is 15.2 ± 0.4%, which is consistent with the value observed previously for Sample Set A 0-h-samples (14.6 ± 0.4%), highlighting that the sample-to-sample variation is <5% (~0.6% in absolute phase fraction).

Table 5: Global GDL/MPL/(PA) phase fractions from 0 h (unoperated) and AST (operated) cells, per electrode for each replicate and mean values.

Sample	Electrode	GDL/MPL/(PA) phase fraction	Mean
0 h (01)	**Anode**	15.9%	16.7%
	Cathode	17.5%	
0 h (02)	**Anode**	15.5%	15.1%
	Cathode	14.7%	
0 h (03)	**Anode**	15.1%	15.4%
	Cathode	15.7%	
0 h (04)	**Anode**	13.8%	13.8%
	Cathode	13.7%	
0 h Mean	**Anode**	15.1%	15.2 ± 0.4%
	Cathode	15.4%	
AST (01)	**Anode**	20.1%	21.3%
	Cathode	22.5%	
AST (02)	**Anode**	25.3%	24.0%
	Cathode	22.6%	
AST (03)	**Anode**	22.6%	23.2%
	Cathode	23.8%	
AST (04)	**Anode**	21.8%	22.2%
	Cathode	22.7%	
AST Mean	**Anode**	22.4%	22.7% ± 0.3%
	Cathode	22.9%	

The equivalent mean and standard error of the mean values for the AST samples were 22.7% and ~0.3%, demonstrating a significant filling of the porous region of the MPL and GDL with leached PA (almost one-third of the pore phase flooded). The mean difference between the two sets (7.4 ± 0.5%) represents an average volumetric increase of ~0.04 mm^3 in each electrode, similar in magnitude to the lifetime testing of Sample Set A (0.05-0.06 mm^3). It is perhaps surprising that this AST, which incorporates current cycling, leads to a similar amount

of PA in the GDL/MPL as operating at a single current density for a similar number of hours (50-100 versus 70 h); suggesting that there is a saturation limit, the current cycling has little added effect over operation time, or that switching between these two current densities has some compensatory effect[51]. More research is required at the flow-field level to understand if in fact the AST causes greater PA egress through the gas channels, whilst nevertheless leaving similar residual PA in the porous electrodes.

The results of areal slice-by-slice analysis are presented in Figure 8. The average measured membrane thicknesses (FWHM) show a more pronounced increase than that observed in lifetime testing, from 44 ± 2 µm in 0-h-samples (Figure 8 a,b,c,d) to 63 ± 1 µm in AST-samples (Figure 8 e,f,g,h), representing on average a 44% increase, far more significant than the internal variation in either case (see **Error! Reference source not found.**). The irreversible swelling observed with this AST is greater in magnitude than the reversible swelling observed in early radiographic studies (20%)[19]. This observation is also contrary to the MEA shrinkage seen in early tomographic literature[25] and indeed implies a volumetric increase despite PA egress. Although only small changes in membrane thickness were detected *in-situ* by a distance sensor in recent work[35], the authors highlight that with the production of large amounts of water at high current densities, protolysis and PA dilution are expected. The impact of *post-mortem* electrochemical testing can be effectively ruled out since these are thought to result in a shrinkage[35], and the same electrochemical tests were carried out for the pristine and operated samples in this study. However, due to the *ex-situ* nature of the investigation, forming small discs for X-ray CT investigation may allow MEA mechanical stresses built up during operation to be relieved by sample sectioning, leading to *post-mortem* deformation. This possibility will be further investigated by lab-based *in-situ* measurements in future work.

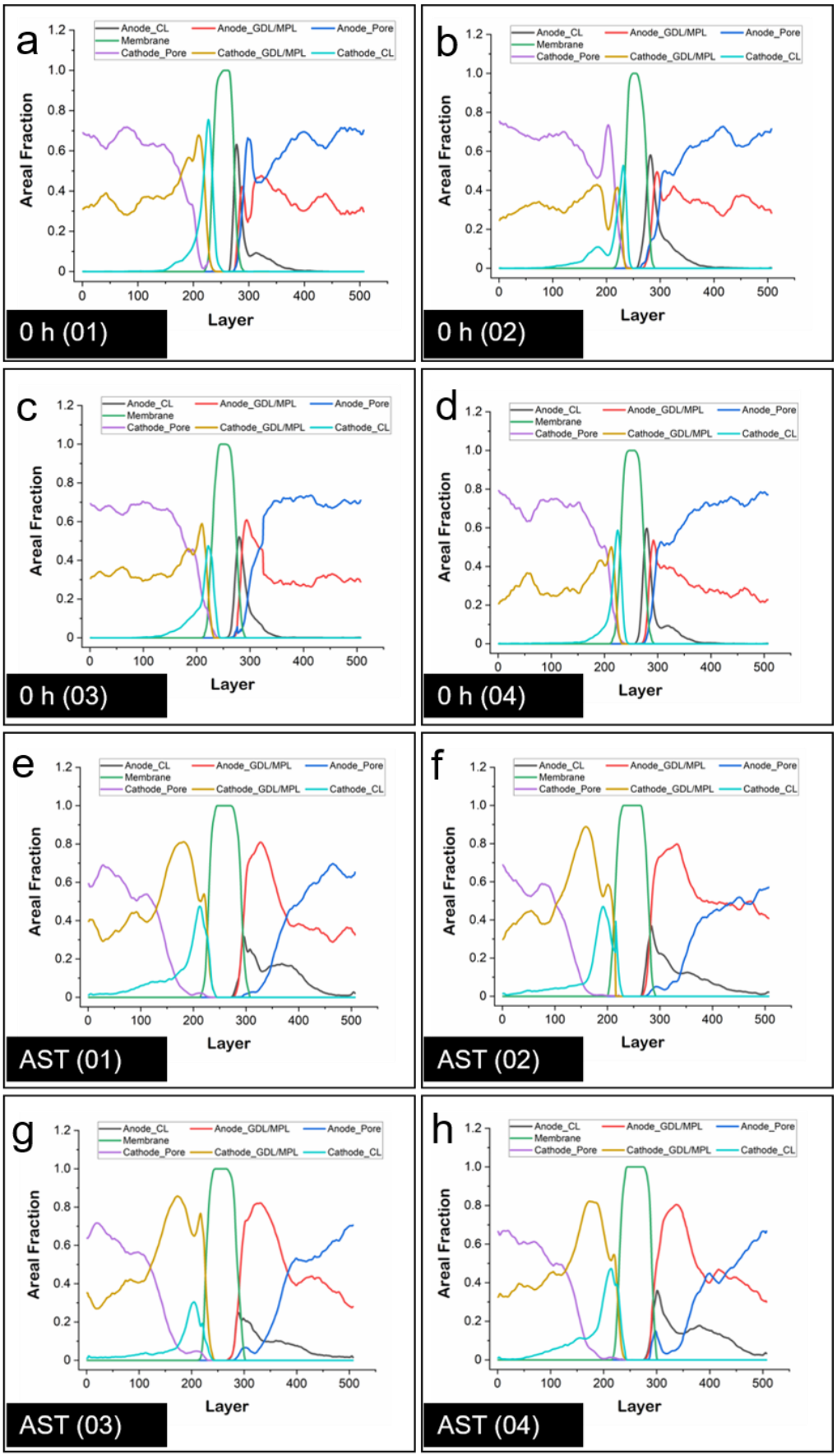

Figure 8: Slice-by-slice plots for Sample Set B, showing the area fraction for each of the seven phases from the cathode *(Layer 1) to the anode (Layer 506)* for (a) 0 h (01); (b) 0 h (02); (c) 0 h (03); (d) 0 h (04); (e) AST (01); (f) AST (02); (g) AST (03); (h) AST (04).

The behaviour of the CL during the AST is also noteworthy. Given that membrane swelling likely accounts for between 14 and 24 µm, if CL migration behaviour during the AST matches the lifetime testing regime, an increase in inter-CL distance of the order of 38 – 48 µm is expected. Indeed, the average inter-CL peak distance in the 0-h- (Figure 8 a,b,c,d) and AST-samples (Figure 8 e,f,g,h) is 54 ± 3 µm and 88 ± 3 µm, respectively, representing a change of between 28 and 41 µm. However, unlike for Sample Set A, the distances between CL peaks and the centre of the membrane are not the same for each electrode in Sample Set B, with a significantly greater migration of the cathode CL (50 µm) than the anode CL (37 µm) (see **Error! Reference source not found.**), suggesting cathodic CL degradation may be greater than anodic CL degradation under the AST regime studied. This would, however, require a more in-depth EIS study or a 3-electrode set-up to experimentally verify, which is beyond the scope of this work.

With regards to PA migration into the MPL/GDL region, the eight samples present a coherent picture which is different from that observed during lifetime testing. In the unoperated cells (Figure 8 a,b,c,d), there is a peak close to the membrane, after the CL, representing the denser MPL layer. After this, the carbonaceous phase fraction generally falls, averaging between 0.27 and 0.34 across all sides and all replicates (overall average 0.30, as for 0-h-samples in Sample Set A). However, in the operated cells (Figure 8 e,f,g,h), rather than the bimodal distribution seen in most electrodes in 50-h- and 100-h-samples, the AST samples present a single large peak at the location attributable to the MPL, without the secondary peak towards where the flow-fields had been. In fact, in all cases there is a depletion of PA as one moves further out from the initial MPL peak. This has been quantified in **Error! Reference source not found.** as the average phase fraction across the first and last 150 slices, where the GDL/MPL/(PA) phase fraction is increased from 0.30 to 0.42 in the GDL region (~41%), a smaller proportional increase versus the entire electrode change (~49%). This may indicate a larger build-up in the MPL region, but that perhaps the PA observed at the outer edges in the lifetime operated cells had escaped *via* the flow-field, giving a similar residual increase in PA

content. Such a hypothesis would require imaging of the flow-field and/or monitoring of the exhaust gases to confirm.

cPSD and τ_z measurements were also performed on both electrodes of each sample, with the cPSD summary shown in Table 6. First, the mean pore size (r_{50} = 12.6 ± 0.4 µm) compares very well with the unoperated cells in Sample Set A (r_{50} = 12.6 ± 0.2 µm), as is expected for these nominally equivalent cells. Again, it is clear there is very little discrepancy between each electrode in these pristine cells. However, there is a small pore size increase after AST, attributable to the greater filling of smaller pores. However, this effect is thought to be less pronounced than that seen during lifetime testing due to the greater concentration of egressed PA in the MPL region which is effectively removed from the analysed volumes here. Therefore, it is likely only the smaller number of small pores found in the GDL being filled that causes the observed change.

Table 6: Summary of Pore cPSD results for Sample Set B

Sample	Electrode	Pore r_{50} (µm)	Mean Pore r_{50} (µm)	An./Cat. Pore r_{50} (µm)
0 h (01)	**Anode**	12.0	11.9	1.01
	Cathode	11.8		
0 h (02)	**Anode**	11.5	11.5	1.00
	Cathode	11.5		
0 h (03)	**Anode**	11.7	13.8	1.01
	Cathode	11.6		
0 h (04)	**Anode**	13.1	13.3	0.97
	Cathode	13.5		
0 h Mean	**Anode**	12.6	12.6 ± 0.4	1.00
	Cathode	12.6		
AST (01)	**Anode**	13.3	14.0	0.91
	Cathode	14.6		
AST (02)	**Anode**	13.7	14.1	0.95
	Cathode	14.5		
AST (03)	**Anode**	12.9	13.4	0.92
	Cathode	13.9		
AST (04)	**Anode**	12.3	13.2	0.87
	Cathode	14.1		
AST Mean	**Anode**	13.0	13.7 ± 0.3	0.91
	Cathode	14.3		

The final column of Table 6 indicates that the average pore size is slightly larger on the cathode side than the anode side, although the interpretation of this result is best examined in conjunction with the tortuosity factor results shown in Table 7.

Table 7: Summary of z-tortuosity factor (τ_z) results for Sample Set B

Sample	Electrode	Pore τ_z	Connectivity	Mean Pore τ_z	Top/Bot. Pore τ_z
0 h (01)	**Anode**	3.34	99.6%	3.2	1.07
	Cathode	3.11	99.5%		
0 h (02)	**Anode**	3.06	99.7%	3.0	1.05
	Cathode	2.92	99.7%		
0 h (03)	**Anode**	2.55	99.9%	2.8	0.84
	Cathode	3.02	99.8%		
0 h (04)	**Anode**	2.86	99.9%	2.7	1.13
	Cathode	2.52	99.9%		
0 h Mean	**Anode**	2.95	99.7%	2.9 ± 0.1	1.02
	Cathode	2.89	99.7%		
AST (01)	**Anode**	3.92	96.9%	3.6	1.21
	Cathode	3.20	97.8%		
AST (02)	**Anode**	4.68	96.6%	4.4	1.12
	Cathode	4.17	97.9%		
AST (03)	**Anode**	5.13	97.9%	4.8	1.17
	Cathode	4.38	97.4%		
AST (04)	**Anode**	5.70	97.0%	4.6	1.60
	Cathode	3.54	98.4%		
AST Mean	**Anode**	4.85	97.1%	4.3 ± 0.3	1.26
	Cathode	3.83	97.9%		

Indeed, a significant increase in tortuosity factor is observed, as well as a consistently higher tortuosity factor for the anode side. Importantly, if the binarized volume is allowed to extend any further towards the MPL region, it rises exponentially for all AST samples, again highlighting significant filling of the MPL. There is also lower connectivity in all AST cases than in the pristine cases, mostly marginally lower in the former on the anode side than the cathode side. From solely the quantity of PA in each GDL, this result would not be apparent, as in most cases the GDL/MPL/(PA) phase fraction is lower on the anode side. Nonetheless, the tortuosity factor calculations run on the binarized GDL layers suggest that either at the GDL/MPL and/or the GDL/flow-field interface, there is greater flooding of PA on the anode side than the cathode side, more greatly hindering gas transport on this electrode. Further investigation to probe the mechanism and establish whether "electrochemical pumping" in this direction is the dominant factor will be the focus of future work.

4 Conclusions

Lifetime and accelerated stress testing of HT-PEFCs have been undertaken, correlating their microstructure and electrochemical performance by combining lab-based X-ray micro-CT and

machine-learning segmentation. Statistically significant changes in the membrane, CL and MPL/GDL, particularly in regard to PA leaching, can be detected and well-characterised without a synchrotron. Although the low-flux, polychromatic lab-source precludes direct *ex-situ* determination of PA location, a multi-sample approach allows ready access to data that can be reliably segmented to yield insights into global and layer-by-layer PA distribution. The following conclusions can be drawn:

i. A laser micro-machining sample preparation route has been developed that can be implemented to provide sufficiently small discs to yield adequate image quality for reliable segmentation by a novel machine-learning based approach. By careful selection of milling parameters, MEA orientation can be retained, giving rise to greater insights into PA leaching anisotropy.

ii. High-fidelity segmented volumes allow for analysis of membrane width, Pt catalyst migration, PA leaching and concomitant changes in the pore networks.

iii. Duplicate lifetime testing shows that the quantity of GDL/MPL-held PA was little changed between 50 h and 100 h, corroborating reports that a steady-state is established within the first few hours. Nonetheless, PA re-distribution likely continues on the order of tens of hours, leading to non-uniform filling. Observed mass transfer polarisation losses correlate well with the recorded microstructural change.

iv. Slice-by-slice analysis of the volumes operated at constant current density identified a bimodal distribution of leached PA, with maxima in the MPL region and towards the outer GDL edge, towards where the flow-fields had been. cPSD and tortuosity factor analysis suggested that smaller pores were filled preferentially, and that with longer operation, a greater disparity in pore network connectivity and tortuosity factor between the two electrodes evolved.

v. Quadruplicate accelerated stress testing showed a similar quantity of leached PA residing in the GDL but with a single, larger maximum at the MPL. This concentration of PA served as a greater barrier to gas transport than the similar quantity of PA in the other tests, resulting in a more significant mass transfer polarisation loss.

vi. cPSD analysis of the GDL region highlighted a less pronounced filling of smaller pores but importantly the z-tortuosity factor was observed to increase, and pore connectivity to decrease, after the AST.

vii. It was also observed that the AST had a much more pronounced impact on membrane swelling and led to less uniform Pt migration across electrodes. However, as discussed in relation to the electrochemical results of Sample Set B, the AST used here likely results in several degradation mechanisms occurring at once. Thus, we stress the need to create standardised, targeted ASTs that are specific to each degradation mechanism and timescale, which would allow for better correlation between electrochemical degradation and changes in MEA morphology observed by X-ray CT.

It is hoped that more research will focus not only on improving the statistical robustness of X-ray CT measurements in electrochemical devices, but that this study has also underlined that a greater understanding of how PA re-distributes within and exits a real cell will help in the design of improved HT-PEFCs. Indeed, the platform developed here has been applied to the application of a PA leaching mitigation approach, which will be the focus of a follow-up publication.

5 Glossary

HT-PEFC – high-temperature polymer electrolyte fuel cell

PBI – polybenzimidazole

PA – phosphoric acid

MEA – membrane electrode assembly

LT-PEFC – low-temperature polymer electrolyte fuel cell

CL – catalyst layer

MPL – microporous layer

CT – computed tomography

GDL – gas diffusion layer

EIS – electrochemical impedance spectroscopy

PNM – pore network model

AST – accelerated stress test

GDE – gas diffusion electrode

PTFE – polytetrafluoroethylene

ADL – acid doping level

CV – cyclic voltammetry

OCV – open-circuit voltage

ECSA – electrochemical surface area

CAD – computer-aided design

VSSA – volume-specific surface area

cPSD – continuous particle size distribution

FWHM – full-width half-maximum

DoE – Department of Energy

6 Acknowledgements

This work has been financially supported by the UK Research Council EPSRC [EP/009050/1],

and JH also acknowledges the EPSRC for her Fellowship [EP/T517793/1].

7 References

[1] J. S. Wainright, J. -T. Wang, D. Weng, R. F. Savinell, and M. Litt, “Acid-Doped Polybenzimidazoles: A New Polymer Electrolyte,” *J. Electrochem. Soc.*, vol. 142, no. 7, pp. L121–L123, 1995, doi: 10.1149/1.2044337.

[2] Q. Li, J. O. Jensen, R. F. Savinell, and N. J. Bjerrum, “High temperature proton exchange membranes based on polybenzimidazoles for fuel cells,” *Prog. Polym. Sci.*, vol. 34, no. 5, pp. 449–477, 2009, doi: 10.1016/j.progpolymsci.2008.12.003.

[3] Q. Li, R. He, J.-A. Gao, J. O. Jensen, and N. J. Bjerrum, “The CO Poisoning Effect in PEMFCs Operational at Temperatures up to 200°C,” *J. Electrochem. Soc.*, vol. 150, no. 12, p. A1599, 2003, doi: 10.1149/1.1619984.

[4] Q. He, X. Yang, W. Chen, S. Mukerjee, B. Koel, and S. Chen, “Influence of phosphate anion adsorption on the kinetics of oxygen electroreduction on low index Pt(hkl) single crystals,” *Phys. Chem. Chem. Phys.*, vol. 12, no. 39, pp. 12544–12555, 2010, doi: 10.1039/c0cp00433b.

[5] A. Kamat, M. Herrmann, D. Ternes, O. Klein, U. Krewer, and S. Scholl, “Experimental investigations into phosphoric acid adsorption on platinum catalysts in a high temperature PEM Fuel cell,” *Fuel Cells*, vol. 11, no. 4, pp. 511–517, 2011, doi: 10.1002/fuce.201000102.

[6] R. Zeis, “Materials and characterization techniques for high-temperature polymer electrolyte membrane fuel cells,” *Beilstein J. Nanotechnol.*, vol. 6, no. 1, pp. 68–83, 2015, doi: 10.3762/bjnano.6.8.

[7] C. Wannek, I. Konradi, J. Mergel, and W. Lehnert, “Redistribution of phosphoric acid in membrane electrode assemblies for high-temperature polymer electrolyte fuel cells,” *Int. J. Hydrogen Energy*, vol. 34, no. 23, pp. 9479–9485, 2009, doi: 10.1016/j.ijhydene.2009.09.076.

[8] R. Bouchet and E. Siebert, “Proton conduction in acid doped polybenzimidazole,” *Solid State Ionics*, vol. 118, no. 3–4, pp. 287–299, 1999, doi: 10.1016/s0167-2738(98)00466-4.

[9] K. A. Perry, K. L. More, E. A. Payzant, R. A. Meisner, B. G. Sumpter, and B. C. Benicewicz, “A comparative study of phosphoric acid-doped m-PBI membranes,” *J. Polym. Sci. Part B Polym. Phys.*, vol. 52, no. 1, pp. 26–35, 2014, doi: 10.1002/polb.23403.

[10] J. Chen, M. Perez-Page, Z. Ji, Z. Zhang, Z. Guo, and S. Holmes, “One step electrochemical exfoliation of natural graphite flakes into graphene oxide for polybenzimidazole composite membranes giving enhanced performance in high temperature fuel cells,” *J. Power Sources*, vol. 491, no. January, p. 229550, 2021, doi: 10.1016/j.jpowsour.2021.229550.

[11] N. Üregen, K. Pehlivanoğlu, Y. Özdemir, and Y. Devrim, “Development of polybenzimidazole/graphene oxide composite membranes for high temperature PEM fuel cells,” *Int. J. Hydrogen Energy*, vol. 42, no. 4, pp. 2636–2647, 2017, doi: 10.1016/j.ijhydene.2016.07.009.

[12] C. Korte, “Phosphoric Acid, an Electrolyte for Fuel Cells – Temperature and Composition Dependence of Vapor Pressure and Proton Conductivity,” in *Fuel Cell Science and Engineering: Materials, Processes, Systems and Technology*, D. S. and B. Emonts, Ed. Weinheim, Germany: Wiley-VCH GmbH & Co. KGaA, 2012, pp. 335–359.

[13] Y. Oono, A. Sounai, and M. Hori, “Influence of the phosphoric acid-doping level in a polybenzimidazole membrane on the cell performance of high-temperature proton exchange membrane fuel cells,” *J. Power Sources*, vol. 189, no. 2, pp. 943–949, 2009, doi: 10.1016/j.jpowsour.2008.12.115.

[14] K. Kwon, T. Y. Kim, D. Y. Yoo, S. G. Hong, and J. O. Park, “Maximization of high-temperature proton exchange membrane fuel cell performance with the optimum distribution of phosphoric acid,” *J. Power Sources*, vol. 188, no. 2, pp. 463–467, 2009, doi: 10.1016/j.jpowsour.2008.11.104.

[15] K. Wippermann, C. Wannek, H. F. Oetjen, J. Mergel, and W. Lehnert, “Cell resistances of poly(2,5-benzimidazole)-based high temperature polymer membrane fuel cell membrane electrode assemblies: Time dependence and influence of operating parameters,” *J. Power Sources*, vol. 195, no. 9, pp. 2806–2809, 2010, doi: 10.1016/j.jpowsour.2009.10.100.

[16] S. Galbiati, A. Baricci, A. Casalegno, and R. Marchesi, “Sensitivity analysis of a polybenzimidazole-based polymer fuel cell and insight into the effect of humidification Samuele,” *Int. J. ENERGY Res.*, vol. 38, pp. 780–790, 2014, doi: 10.1002/er.

[17] N. Pilinski, M. Rastedt, and P. Wagner, “Investigation of Phosphoric Acid Distribution in PBI Based HT-PEM Fuel Cells,” *ECS Trans.*, vol. 69, no. 17, pp. 323–335, 2015, doi: 10.1149/06917.0323ecst.

[18] K. Kwon, J. O. Park, D. Y. Yoo, and J. S. Yi, “Phosphoric acid distribution in the membrane electrode assembly of high temperature proton exchange membrane fuel cells,” *Electrochim. Acta*, vol. 54, no. 26, pp. 6570–6575, 2009, doi: 10.1016/j.electacta.2009.06.031.

[19] W. Maier *et al.*, “In-situ synchrotron X-ray radiography on high temperature polymer electrolyte fuel cells,” *Electrochem. commun.*, vol. 12, no. 10, pp. 1436–1438, 2010, doi: 10.1016/j.elecom.2010.08.002.

[20] W. Maier *et al.*, “Investigation of HT-PEFCs by means of synchrotron X-ray radiography and electrochemical impedance spectroscopy,” *ECS Trans.*, vol. 41, no. 1, pp. 1413–1422, 2011, doi: 10.1149/1.3635672.

[21] R. Kuhn *et al.*, “Measuring device for synchrotron X-ray imaging and first results of high temperature polymer electrolyte membrane fuel cells,” *J. Power Sources*, vol. 196, no. 12, pp. 5231–5239, 2011, doi: 10.1016/j.jpowsour.2010.11.025.

[22] W. Maier *et al.*, “Correlation of synchrotron X-ray radiography and electrochemical impedance spectroscopy for the investigation of HT-PEFCs,” *J. Electrochem. Soc.*, vol. 159, no. 8, pp. F398–F404, 2012, doi: 10.1149/2.024208jes.

[23] A. Tobias *et al.*, “Synchrotron X-ray radioscopic in situ study of high-temperature polymer electrolyte fuel cells - Effect of operation conditions on structure of membrane,” *J. Power Sources*, vol. 246, pp. 290–298, 2014, doi: 10.1016/j.jpowsour.2013.07.094.

[24] S. H. Eberhardt, F. Marone, M. Stampanoni, F. N. Büchi, and T. J. Schmidt, “Quantifying phosphoric acid in high-temperature polymer electrolyte fuel cell components by X-ray tomographic microscopy,” *J. Synchrotron Radiat.*, vol. 21, no. 6, pp. 1319–1326, 2014, doi: 10.1107/S1600577514016348.

[25] S. H. Eberhardt, M. Toulec, F. Marone, M. Stampanoni, F. N. Büchi, and T. J. Schmidt, “Dynamic operation of HT-PEFC: In-operando imaging of phosphoric acid profiles and (re)distribution,” *J. Electrochem. Soc.*, vol. 162, no. 3, pp. F310–F316, 2015, doi: 10.1149/2.0751503jes.

[26] H. R. Kunz, “Lessons Learned from Phosphoric Acid Electrolyte Fuel Cell Development Pertinent to PEMFCs,” *ECS Trans.*, vol. 11, no. 1, pp. 1447–1460, 2019, doi: 10.1149/1.2781058.

[27] J. Halter, F. Marone, and T. J. Schmidt, “Breaking through the Cracks : On the Mechanism of Phosphoric Acid Migration in High Temperature Polymer Electrolyte Fuel,” vol. 165, no. 14, pp. 1176–1183, 2018, doi: 10.1149/2.0501814jes.

[28] S. Chevalier *et al.*, “Role of the microporous layer in the redistribution of phosphoric acid in high temperature PEM fuel cell gas diffusion electrodes,” *Electrochim. Acta*, vol. 212, pp. 187–194, 2016, doi: 10.1016/j.electacta.2016.06.121.

[29] J. Gostick *et al.*, “OpenPNM: A Pore Network Modeling Package,” *Comput. Sci. Eng.*, vol. 18, no. 4, pp. 60–74, 2016, doi: 10.1109/MCSE.2016.49.

[30] D. Wilkinson and J. F. Willemsen, “Invasion percolation: A new form of percolation theory,” *J. Phys. A. Math. Gen.*, vol. 16, no. 14, pp. 3365–3376, 1983, doi: 10.1088/0305-4470/16/14/028.

[31] L. Vásárhelyi, Z. Kónya, Kukovecz, and R. Vajtai, “Microcomputed tomography–based characterization of advanced materials: a review,” *Mater. Today Adv.*, vol. 8, pp. 1–13, 2020, doi: 10.1016/j.mtadv.2020.100084.

[32] S. Carmignato, W. Dewulf, and R. Leach, *Industrial X-ray computed tomography*. 2017.

[33] V. Cnudde, B. Masschaele, M. Dierick, J. Vlassenbroeck, L. Van Hoorebeke, and P. Jacobs, “Recent progress in X-ray CT as a geosciences tool,” *Appl. Geochemistry*, vol. 21, no. 5, pp. 826–832, 2006, doi: 10.1016/j.apgeochem.2006.02.010.

[34] F. Mack *et al.*, “Morphology studies on high-temperature polymer electrolyte membrane fuel cell electrodes,” *J. Power Sources*, vol. 255, pp. 431–438, 2014, doi: 10.1016/j.jpowsour.2014.01.032.

[35] D. Schonvogel, M. Rastedt, P. Wagner, M. Wark, and A. Dyck, “Impact of Accelerated Stress Tests on High Temperature PEMFC Degradation,” *Fuel Cells*, vol. 16, no. 4, pp. 480–489, 2016, doi: 10.1002/fuce.201500160.

[36] J. Halter, T. Gloor, B. Amoroso, T. J. Schmidt, and F. N. Büchi, “Wetting properties of porous high temperature polymer electrolyte fuel cells materials with phosphoric acid,” *Phys. Chem. Chem. Phys.*, vol. 21, no. 24, pp. 13126–13134, 2019, doi: 10.1039/c9cp02149c.

[37] J. Halter, N. Bevilacqua, R. Zeis, T. J. Schmidt, and F. N. Büchi, “The impact of the catalyst layer structure on phosphoric acid migration in HT-PEFC – An operando X-ray tomographic microscopy study,” *J. Electroanal. Chem.*, vol. 859, p. 113832, 2020, doi: 10.1016/j.jelechem.2020.113832.

[38] J. Hack *et al.*, “X-ray Micro-Computed Tomography of Polymer Electrolyte Fuel Cells: What is the Representative Elementary Area?,” *J. Electrochem. Soc.*, vol. 167, no. 1, p. 013545, 2020, doi: 10.1149/1945-7111/ab6983.

[39] I. V. Zenyuk, D. Y. Parkinson, L. G. Connolly, and A. Z. Weber, “Gas-diffusion-layer structural properties under compression via X-ray tomography,” *J. Power Sources*, vol. 328, pp. 364–376, 2016, doi: 10.1016/j.jpowsour.2016.08.020.

[40] K. Yezerska *et al.*, “Characterization methodology for anode starvation in HT-PEM fuel cells,” *Int. J. Hydrogen Energy*, vol. 44, no. 33, pp. 18330–18339, 2019, doi: 10.1016/j.ijhydene.2019.05.114.

[41] L. A. Feldkamp, L. C. Davis, and J. W. Kress, “Practical cone-beam algorithm,” *J. Opt. Soc. Am. A*, vol. 1, no. 6, pp. 612–619, 1984, doi: 10.1364/JOSAA.1.000612.

[42] C. Sommer, C. Straehle, U. Kothe, and F. A. Hamprecht, “Ilastik: Interactive learning and segmentation toolkit,” *Proc. - Int. Symp. Biomed. Imaging*, pp. 230–233, 2011, doi: 10.1109/ISBI.2011.5872394.

[43] T. F. Scientific, *Avizo Software 9 User’s Guide*, vol. 9. 2018.

[44] J. Halter, N. Bevilacqua, R. Zeis, T. J. Schmidt, and F. N. Büchi, “The impact of the catalyst layer structure on phosphoric acid migration in HT-PEFC – An operando X-ray tomographic microscopy study,” *J. Electroanal. Chem.*, p. 113832, 2020, doi: 10.1016/j.jelechem.2020.113832.

[45] S. J. Cooper, A. Bertei, P. R. Shearing, J. A. Kilner, and N. P. Brandon, “TauFactor: An open-source application for calculating tortuosity factors from tomographic data,” *SoftwareX*, vol. 5, pp. 203–210, 2016, doi: 10.1016/j.softx.2016.09.002.

[46] B. Münch and L. Holzer, “Contradicting Geometrical Concepts in Pore Size Analysis Attained with Electron Microscopy and Mercury Intrusion,” *J. Am. Ceram. Soc.*, vol. 91, no. 12, pp. 4059–4067, 2008, doi: 10.1111/j.1551-2916.2008.02736.x.

[47] “DoE Fuel Cell Targets,” 2020. https://www.energy.gov/eere/fuelcells/doe-technical-targets-polymer-electrolyte-membrane-fuel-cell-components.

[48] S. Yu, L. Xiao, and B. C. Benicewicz, “Durability studies of PBI-based high temperature PEMFCs,” *Fuel Cells*, vol. 8, no. 3–4, pp. 165–174, 2008, doi: 10.1002/fuce.200800024.

[49] C. Wannek, B. Kohnen, H. F. Oetjen, H. Lippert, and J. Mergel, “Durability of ABPBI-based MEAs for high temperature PEMFCs at different operating conditions,” *Fuel Cells*, vol. 8, no. 2, pp. 87–95, 2008, doi: 10.1002/fuce.200700059.

[50] L. Xiao *et al.*, “High-temperature polybenzimidazole fuel cell membranes via a sol-gel

process,” *Chem. Mater.*, vol. 17, no. 21, pp. 5328–5333, 2005, doi: 10.1021/cm050831+.

[51] J. Halter, S. Thomas, S. K. Kær, T. J. Schmidt, and F. N. Büchi, “The influence of phosphoric acid migration on the performance of high temperature polymer electrolyte fuel cells,” *J. Power Sources*, vol. 399, no. July, pp. 151–156, 2018, doi: 10.1016/j.jpowsour.2018.07.090.